Development of the Navy's 3D Mine Impact Burial Prediction Model (IMPACT35)

Dr. Peter C Chu, LCDR Ashley Evans, LCDR Anthony Gilles, LCDR Timothy Smith, and LCDR Victoria Taber
Naval Ocean Analysis and Prediction Laboratory, Oceanography Department
Naval Postgraduate School, Monterey, California, USA

Atract-- Falling of mine through air, water, and sediment is investigated experimentally and theoretically. Two experiments were conducted to drop cylindrical mine with the density ratio around 1.8 into shallow water (around 13 m deep) in the Monterey Bay (Exp-1) and into the Naval Postgraduate School's swimming pool (Exp-2). During the experiments, we carefully observe mine track and burial depth while simultaneously taking gravity cores (in Exp-1). After analyzing the gravity cores, we obtain the bottom sediment density and shear strength profiles. The theoretical work includes the development of 3D mine impact burial prediction model (IMPACT35) which contains three components: triple coordinate transform, hydrodynamics of falling rigid object in a single medium (air, water, or sediment) and in multiple media (air-water and water-sediment interfaces). The model predicts the rigid body's trajectory in the water column and burial depth and orientation in the sediment. The experimental data (burial depth, sediment density and shear strength) are used to evaluate the newly developed numerical model. The 3D model shows great improvement to the currently used US Navy's 2D model (i.e., IMPACT28).

1. Introduction

The conclusion of the cold war culminated with the Union of Soviet Socialist Republics (USSR) effectively ceasing to exist under international law on December 31, 1991. This historical event caused the U.S. military and specifically the Navy and Marine Corp Team to shift tactical emphasis from blue water, deep ocean doctrine to littoral warfare doctrine. This shift predicated military responses dealing with a wide range of worldwide regional crises requiring forward sea basing, and expeditionary force landing support.

The Navy Marine Corp team developed a doctrine concept white paper, "… From the Sea, 1992", to support joint warfare doctrine concepts of forward presence and engagement developed as National Defense Strategy in "Joint Vision 2010, 1996", (Rhodes and Holder 1998). The document provided guiding tenets for naval operations of the 21st century. A subsequent Naval Department revision, "Forward …From the Sea, 1994", and its Marine Corp counterparts "Operational Maneuver from the Sea, 1996", and "Ship to Objective Maneuver, 1997" all focus on sea based power projection into littoral regions and guiding naval operations in those areas in the new millennium. "Joint Vision 2020, 2000" and "Sea Strike, Sea Shield, Sea Basing, 2002" are the current National Defense Strategy and Naval Department concept papers providing guiding tenets for naval and joint operations well into the 21st century. Both papers incorporate emerging technology, processes, people and organizations synergized via the netcentric warfare concept to provide total power projection and dominance across littoral regions during any crises requiring U.S. response.

> ...the very shallow water (VSW) region is a critical point for our offensive forces and can easily, quickly and cheaply be exploited by the enemy. The magnitude of the current deficiency in reconnaissance and neutralization in these regions and the impact on amphibious assault operations were demonstrated during Operation Desert Storm. Maj. Gen. Edward J. Hanlon Jr. "From (Rhodes and Holder 1998)."

Any military operation that occurs in the littoral regions also occurs in mine country. The increasing pace of shallow-water naval operations (i.e. Persian Gulf, Adriatic Sea, Yellow Sea, and Gulf of Aden) translates into a high probability of encountering mines. The required shift in focus of naval operations from the open ocean to the regional littoral areas increases the importance of mine warfare as a navy core competency. The proliferation of inexpensive, bottom type mines make shallow water and very shallow water MCM a critical and expensive challenge. In times of conflict domination of coastal operating areas will largely depend on the ability to remove

Manuscript received January 15, 2004. This work was supported by the U.S. Office of Naval Research, Naval Oceanographic Office, and Naval Postgraduate School.

Peter C. Chu is with the Naval Postgraduate School, Monterey, CA 93943 USA (telephone: 831-677-3688, e-mail: chu@ nps.navy.mil).

or neutralize any emplaced littoral mine threat, figure 1, and prepare the battle space for follow-on action in a timely fashion Naval mines may be found throughout the water column and on or within the seafloor. Ask anyone to describe a typical naval mine to you and the response will be a description of the spherical, hertz-horn World War II vintage drifting mine shape common in Hollywood films. But, it is the buried naval mine that poses the most severe threat to naval assets since naval forces possess very limited resources and capabilities for detecting, identifying, and neutralizing them, and the mine itself remains fully effective when buried, (Lott, 2001). An important factor in mine hunting and clearance is the amount of initial impact and subsequent sediment burial a mine undergoes with time because buried mines are substantially more difficult to detect and classify. The amount of burial becomes a critical parameter and crossroad in the naval MCM mission planning process because the mine countermeasures effort transitions from mine hunting to mine sweeping, (Rennie 2002.) Littoral Mine Threat. "From (Rhodes 1998)."

> Mine warfare, perhaps more than any other single littoral warfare mission area is the "key" that will unlock the "door" to the littoral battle space. In the most fundamental way, then, mine warfare and the need for effective mine countermeasures must be an "all-hands" concern for the Navy and the Marine Corps. (Boorda 1995)

Fig.1. Littoral Zone Mine Treat (from Rhodes 1998).

The Office of Naval Research (ONR) in 1999 created the Mine Burial Program (MBP), an applied (6.2) research program to develop mine burial prediction tools and decision aids. The program mission is to predict the behavior of mines in different environments, (Bennett 2000). The Impact Mine Burial Prediction model development falls under the MBP program.

The Impact Mine Burial Prediction model developed in 1980 was developed to semi-empirically model the mine burial process. Several revisions have occurred in the last two decades but there have been limitations noted in the model performance, as well as little scientific advancement in mine burial prediction, (Dolan et al 1999), (Taber 1999), (Smith 2000), and (Gilless 2001).

In this study, a nonlinear dynamical system (IMPACT35) is established for the movement of a nonuniform (center of gravity not the same as the center of volume) mine through the water-sediment interface. A cylinder-drop experiment was conducted. The data collected from the experiment can be used for model development and verification. The long-term goal is for model inclusion in a full spectrum deterministic model for mine burial in a comprehensive navy tactical decision aid.

2. Triple Coordinate Systems

Consider an axially symmetric cylinder with the centers of mass (COM) **X** [or called gravity center (GC) in literatures] and center of volume (COV) **B** on the main axis (Fig. 2a). Let (L, R, χ) represent the cylinder's length, radius, and the distance between the two points (**X**, **B**). The positive χ-values refer to nose-down case, i.e., the point **X** is lower than the point **B**. Three coordinate systems are used to model the falling cylinder through the air, water, and sediment phases: earth-fixed coordinate (E-coordinate), main-axis following coordinate (M-coordinate), and force following coordinate (F-coordinate) systems. All the systems are three-dimensional, orthogonal, and right-handed ([2] Chu et al. 2004).

The E-coordinate is represented by F_E(O, i, j, k) with the origin 'O', and three axes: x-, y- axes (horizontal) with the unit vectors (i, j) and z-axis (vertical) with the unit vector k (upward positive). The position of the cylinder is represented by the COM position,

$$\mathbf{X} = x\mathbf{i} + y\mathbf{j} + z\mathbf{k}. \tag{1}$$

The translation velocity is given by

$$\frac{d\mathbf{X}}{dt} = \mathbf{V}, \qquad \mathbf{V} = (u, v, w). \tag{2}$$

Let orientation of the cylinder's main-axis (pointing downward) is given by i_M, and ψ_1 be the angle that the cylinder rotates around the axis i_M. The angle between i_M and k is denoted by $\psi_2 + \pi/2$. Here, ψ_2 is usually called the elevation angle. Projection of the vector i_M onto the (x, y) plane creates angle (ψ_3) between the projection and the x-axis (Fig. 2b). The M-coordinate is represented by F_M(X, i_M, j_M, k_M) with the origin 'X', unit vectors (i_M, j_M, k_M), and coordinates ($x^{(m)}$, $y^{(m)}$, $z^{(m)}$). The unit vectors of the M-coordinate system are given by (Fig. 2b)

$$\mathbf{j}_M = \mathbf{k} \times \mathbf{i}_M, \qquad \mathbf{k}_M = \mathbf{i}_M \times \mathbf{j}_M \tag{3}$$

The M-coordinate system is solely determined by orientation of the cylinder's main-axis $\mathbf{i}_M$.

The F-coordinate is represented by $F_F(\mathbf{X}, \mathbf{i}_F, \mathbf{j}_F, \mathbf{k}_F)$ with the origin $\mathbf{X}$, unit vectors ($\mathbf{i}_F$, $\mathbf{j}_F$, $\mathbf{k}_F$), and coordinates ($x^{(F)}$, $y^{(F)}$, $z^{(F)}$). Let V_w be the fluid velocity. The water-to-cylinder velocity is represented by

$$\mathbf{V}_r = \mathbf{V}_w - \mathbf{V}, \tag{4}$$

which can be decomposed into two parts,

$$\mathbf{V}_r = \mathbf{V}_1 + \mathbf{V}_2, \mathbf{V}_1 = (\mathbf{V}_r \cdot \mathbf{i}_F)\mathbf{i}_F, \mathbf{V}_2 = \mathbf{V}_r - (\mathbf{V}_r \cdot \mathbf{i}_F)\mathbf{i}_F \tag{5}$$

where $\mathbf{V}_1$ is the component paralleling to the cylinder's main-axis (i.e., along $\mathbf{i}_M$), and $\mathbf{V}_2$ is the component perpendicular to the cylinder's main-axial direction. The unit vectors for the F-coordinate are defined by (column vectors)

$$\mathbf{i}_F = \mathbf{i}_M, \qquad \mathbf{j}_F = \mathbf{V}_2/|\mathbf{V}_2|, \qquad \mathbf{k}_F = \mathbf{i}_F \times \mathbf{j}_F. \tag{6}$$

3. Dynamics

3.1. Momentum Balance

The translation velocity of the cylinder ($\mathbf{V}$) is governed by the momentum equation in the E-coordinate system,

$$\frac{d}{dt}\begin{bmatrix} u \\ v \\ w \end{bmatrix} = -\begin{bmatrix} 0 \\ 0 \\ g \end{bmatrix} + \frac{\mathbf{F}_b + \mathbf{F}_h}{\rho \Pi}, \tag{7}$$

where g is the gravitational acceleration; $\mathbf{F}_b$ is the buoyancy force; Π is the cylinder volume; ρ is the rigid body density; $\rho \Pi = m$, is the cylinder mass; $\mathbf{F}_h$ is the hydrodynamic force (i.e., surface force including drag, lift, impact forces). The drag and lift forces are calculated using the drag and lift laws with the given water-to-cylinder velocity ($\mathbf{V}_r$). In the F-coordinate, $\mathbf{V}_r$ is decomposed into along-cylinder ($\mathbf{V}_1$) and across-cylinder ($\mathbf{V}_2$) components.

3.2. Moment of Momentum Equation

It is convenient to write the moment of momentum equation

$$\mathbf{J} \bullet \frac{d\boldsymbol{\omega}}{dt} = \mathbf{M}_b + \mathbf{M}_h, \tag{8}$$

in the M-coordinate system with the cylinder's angular velocity components $(\omega_1, \omega_2, \omega_3)$ defined by (4). The gravity force, passing the COM, doesn't induce the moment. $\mathbf{M}_b$ and $\mathbf{M}_h$ are the buoyancy and hydrodynamic force torques. In the M-coordinate system, the moment of gyration tensor for the axially symmetric cylinder is a diagonal matrix

$$\mathbf{J} = \begin{bmatrix} J_1 & 0 & 0 \\ 0 & J_2 & 0 \\ 0 & 0 & J_3 \end{bmatrix}, \tag{9}$$

where J_1, J_2, and J_3 are the moments of inertia. The gravity force, passing the center of mass, doesn't induce the moment. The buoyancy force induces the moment in the $\mathbf{j}_M$ direction if the COM doesn't coincide with the COV (i.e., $\chi \neq 0$),

$$\mathbf{M}_b = |\mathbf{F}_b| \chi \cos\psi_2 \mathbf{j}_M. \tag{10}$$

Computation of buoyancy and hydrodynamic forces ($\mathbf{F}_b$, $\mathbf{F}_h$) and torques ($\mathbf{M}_b$, $\mathbf{M}_h$) is more complicated for a cylinder penetrating through air-water and water-sediment interfaces than falling through a single medium such as water. At the instance when the cylinder penetrates into an interface, three situations may exist: one-side entry with the lower surface partially contacting the interface (Fig. 3a), one-side entry with partial area with the lower surface completely inside the lower medium (Fig. 3b), and two-side entry (Fig. 3c). For the two-side penetration, the upper (above the interface) and lower (below the interface) parts of the cylinder are represented by $D^{(1)}$ and $D^{(2)}$. For the one-side penetration, the upper (or lower) part of the cylinder are considered as the combination of $D^{(1)}$ [or $D^{(2)}$] and a sub-cylinder $C^{(1)}$ [or $C^{(2)}$]. In general, the upper and lower parts of the cylinder are represented by [$C^{(1)}$, $D^{(1)}$] and [$C^{(2)}$, $D^{(2)}$]. For the two-side penetration, $C^{(1)} = C^{(2)} = 0$.

4. Buoyancy Force

Let (L_c, L_m) be the lengths of [$C^{(1)}$, $D^{(1)}$], (h_1, h_2) the heights of the two sides of $D^{(1)}$, ($\mathbf{F}_b^{(1)}$, $\mathbf{F}_b^{(2)}$) the buoyancy forces for the upper and lower parts of the cylinder (Fig. 4). The vertical cross-section of $D^{(1)}$ is shown in Fig. 5. In the M-coordinate system, we have

$$s(x^{(m)}) = R^2 \cos^{-1}\left(1 - \frac{h_1}{R} - \frac{\Delta h}{L_m R} x^{(m)}\right) - \left(R - h_1 - \frac{\Delta h}{L} x^{(m)}\right)\sqrt{R - \left(R - h_1 - \frac{\Delta h}{L} x^{(m)}\right)^2}, \tag{11}$$

where $\Delta h = h_2 - h_1$. The integration of $s(x)$ along $x^{(m)}$ axis gives the volume of $D^{(1)}$,

$$\Pi^{(1)} = \int_0^{L_m} s(x^{(m)}) dx^{(m)} = \frac{R^3 L_m}{\Delta h} \beta(\kappa_1, \kappa_2), \tag{12}$$

where

$$\beta(\kappa_1, \kappa_2) \equiv \kappa_1 \cos^{-1}(\kappa_1) - \sqrt{1 - \kappa_1^2} + \frac{1}{3}\left(1 - \kappa_1^2\right)^{\frac{3}{2}} - \kappa_2 \cos^{-1}(\kappa_2) + \sqrt{1 - \kappa_2^2} - \frac{1}{3}\left(1 - \kappa_2^2\right)^{\frac{3}{2}},$$

$$\kappa_1 = 1 - h_1 / R,\ \ \kappa_2 = 1 - h_2 / R\,. \tag{13}$$

The volume of $C^{(1)}$ is calculated by

$$\Omega^{(1)} = \pi R^2 L_c\,. \tag{14}$$

The buoyancy force $\mathbf{F}_b^{(1)}$ is the product of the medium (air, water, or sediment) density and volume $\Pi^{(1)} + \Omega^{(1)}$,

$$\begin{aligned}\mathbf{F}_b^{(1)} &= \rho^{(1)}(\Pi^{(1)} + \Omega^{(1)})\mathbf{k} \\ &= \rho^{(1)}\left[\frac{R^3 L_m}{\Delta h}\beta(\kappa_1,\kappa_2) + \pi R^2 L_c\right]\mathbf{k}.\end{aligned} \tag{15}$$

The volume of the lower part of the cylinder [$C^{(2)}$, $D^{(2)}$] is given by

$$\Pi^{(2)} + \Omega^{(2)} = \pi R^2 L - \Pi^{(1)} - \Omega^{(1)}\,. \tag{16}$$

The buoyancy force $\mathbf{F}_b^{(2)}$ is calculated by

$$\mathbf{F}_b^{(2)} = \rho^{(2)}\left(\Pi^{(2)} + \Omega^{(2)}\right)\mathbf{k}. \tag{17}$$

Substitution of (15) and (16) into (17) leads to

$$\mathbf{F}_b^{(2)} = \rho^{(2)}\left[\pi R^2 (L - L_c) - \frac{R^3 L_m}{\Delta h}\beta(\kappa_1,\kappa_2)\right]\mathbf{k}. \tag{18}$$

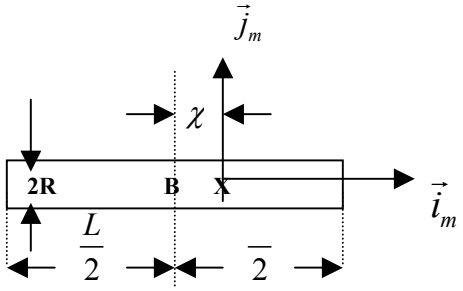

Fig. 2a. M-coordinate with the COM as the origin X and (i_m, j_m) as the two axes. Here, χ is the distance between the COV (B) and COM, (L, R) are the cylinder's length and radius.

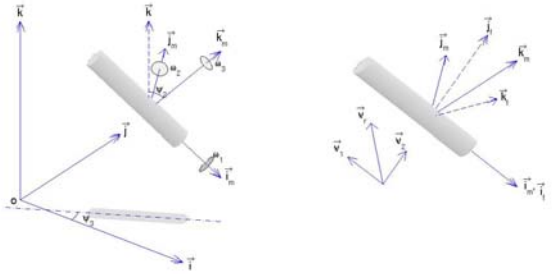

Fig. 2b. Three coordinate systems.

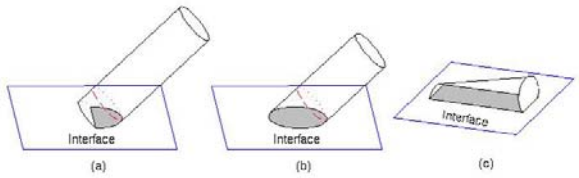

Fig. 3. (a) One-side entry with the lower surface partially contacting the interface, (b) one-side entry with partial area with the lower surface completely inside the lower medium, and (c) two-side entry.

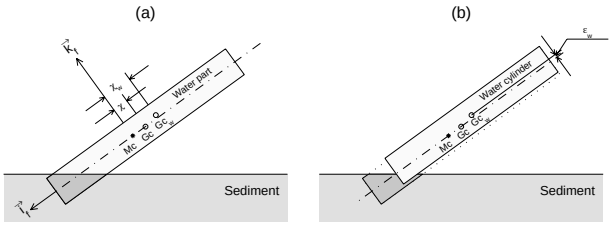

Fig. 4. Equivalent cylinder method for computing buoyancy force and torque of the volume above the interface.

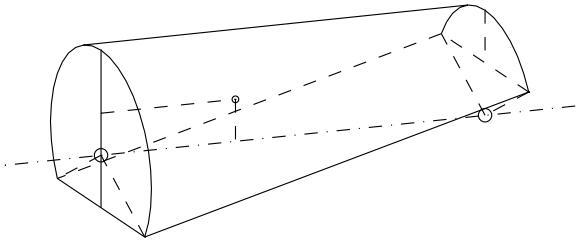

Fig. 5. Geometry of the part $D^{(1)}$.

5. Torque due to the Buoyancy Force

The torque due to the buoyancy force should be calculated separately for the upper and lower parts of the cylinder as it penetrates the interface. Here, we use the upper part as the illustration. Let $(x_B^{(1)}, z_B^{(1)})$ be the COV_1 location of the upper part of the cylinder in the M-coordinate system. Note that the origin of the M-coordinate is the COM of the cylinder. The location of COV_1 is defined by

$$(x_B^{(1)}, z_B^{(1)}) = \frac{1}{\Pi^{(1)} + \Omega^{(1)}} \left[\begin{array}{l} \iiint (x^{(m)}, z^{(m)}) d\Pi^{(1)} \\ + \iiint (x^{(m)}, z^{(m)}) d\Omega^{(1)} \end{array} \right]$$

$$= \frac{1}{\Pi^{(1)} + \Omega^{(1)}} \left[\int_0^{L_m} (x^{(m)}, z^{(m)}) s(x^{(m)}) dx^{(m)} + (\frac{L_c}{2}, 0)\Omega^{(1)} \right] \quad (19)$$

Substitution of (11), (12) and (14) into (19) leads to

$$x_B^{(1)} = \frac{R\Delta h}{\beta(\kappa_1, \kappa_2) L_m (1 + \pi \Delta h L_c \beta^{-1} L_m^{-1})} \left[\begin{array}{l} \left(\frac{L_m}{\Delta h} \right)^2 \mu_x(\kappa_1, \kappa_2) \\ + \frac{1}{2} \left(\frac{L_c}{R} \right)^2 \end{array} \right], \quad (20)$$

$$z_B^{(1)} = \frac{R}{6\beta(\kappa_1, \kappa_2)(1 + \pi \Delta h L_c \beta^{-1} L_m^{-1})} \mu_z(\kappa_1, \kappa_2), \quad (21)$$

where

$$\mu_x(\kappa_1, \kappa_2) \equiv \frac{1}{4} \left[\begin{array}{l} \left(2\kappa_2^2 - 1\right) \cos^{-1} \kappa_2 - \left(2\kappa_1^2 - 1\right) \cos^{-1} \kappa_1 \\ + \kappa_1 \sqrt{1 - \kappa_1^2} - \kappa_2 \sqrt{1 - \kappa_2^2} \end{array} \right]$$
$$+ \frac{1}{4} \left[\kappa_2 \sqrt{\left(1 - \kappa_2^2\right)^3} - \kappa_1 \sqrt{\left(1 - \kappa_1^2\right)^3} \right]$$
$$- \frac{1}{8} \left(\kappa_2 \sqrt{1 - \kappa_2^2} - \kappa_1 \sqrt{1 - \kappa_1^2} + \sin^{-1} \kappa_2 - \sin^{-1} \kappa_1 \right)$$
$$- \kappa_1 \left(\kappa_2 \cos^{-1} \kappa_2 - \kappa_1 \cos^{-1} \kappa_1 + \sqrt{1 - \kappa_1^2} - \sqrt{1 - \kappa_2^2} \right)$$
$$- \frac{\kappa_1}{3} \left[\sqrt{\left(1 - \kappa_2^2\right)^3} - \sqrt{\left(1 - \kappa_1^2\right)^3} \right],$$

$$\mu_z(\kappa_1, \kappa_2) \equiv \kappa_1 \sqrt{\left(1 - \kappa_1^2\right)^3} - \kappa_2 \sqrt{\left(1 - \kappa_2^2\right)^3}$$
$$+ \frac{3}{2} \left(\kappa_1 \sqrt{1 - \kappa_1^2} - \kappa_2 \sqrt{1 - \kappa_2^2} + \sin^{-1} \kappa_1 - \sin^{-1} \kappa_2 \right) \quad (22)$$

The distance between COM and COV_1 is calculated by

$$\chi^{(1)} = \sqrt{[x_B^{(1)}]^2 + [z_B^{(1)}]^2} \quad (23)$$

The torque due to the buoyancy force for the upper part is given by [see (10]

$$\mathbf{M}_b^{(1)} = \left| \mathbf{F}_b^{(1)} \right| \chi^{(1)} \cos \psi_2 \mathbf{j}_M. \quad (24)$$

Substitution of (18) and (23) into (24) leads to

$$\mathbf{M}_b^{(1)} = \rho^{(1)} \left[\begin{array}{l} \frac{R^3 L_m}{\Delta h} \beta(\kappa_1, \kappa_2) \\ + \pi R^2 L_c \end{array} \right] \sqrt{[x_B^{(1)}]^2 + [z_B^{(1)}]^2} \cos \psi_2 \mathbf{j}_M. \quad (25)$$

The torque due to the buoyancy force for the lower part of the cylinder can be calculated using the same procedure.

6. Hydrodynamic Force and Torque for Air and Water

Let $(\sigma^{(1)}, \sigma^{(2)})$ be the surface of the upper and lower parts of the cylinder. During the penetration, the total hydrodynamic force and associated torque are decomposed into upper and lower parts,

$$\mathbf{F}_h = \mathbf{F}_h^{(1)} + \mathbf{F}_h^{(2)}, \quad \mathbf{M}_h = \mathbf{M}_h^{(1)} + \mathbf{M}_h^{(2)}, \quad (26)$$

where $(\mathbf{F}_h^{(1)}, \mathbf{M}_h^{(1)})$ and $(\mathbf{F}_h^{(2)}, \mathbf{M}_h^{(2)})$ are the force and torque on the upper and lower surfaces $\sigma^{(1)}$ and $\sigma^{(2)}$. Let the hydrodynamic force be $\mathbf{f}_h$ at a point $\mathbf{r}$ (represented in M-coordinate) on the cylinder's surface, the hydrodynamic forces and torques are calculated by

$$\begin{array}{l} \mathbf{F}_h^{(1)} = \iint_{\sigma_1} \mathbf{f}_h d\sigma, \quad \mathbf{F}_h^{(2)} = \iint_{\sigma_2} \mathbf{f}_h d\sigma, \\ \mathbf{M}_h^{(1)} = \iint_{\sigma_1} (\mathbf{r} \times \mathbf{f}_h) d\sigma, \quad \mathbf{M}_h^{(2)} = \iint_{\sigma_2} (\mathbf{r} \times \mathbf{f}_h) d\sigma \end{array}. \quad (27)$$

The hydrodynamic force and torque for air and water are calculated using the recursive model recently developed ([2] Chu et al., 2004). However, the surface force and torque due to sediment should be computed separately.

7. Hydrodynamic Force and Torque for Sediment

Let $\mathbf{v}$ be the velocity at point $\mathbf{r}$ on the cylinder surface,

$$\mathbf{v} = \mathbf{V} + \boldsymbol{\omega} \times \mathbf{r}.$$

The velocity ($\mathbf{v}$) and hydrodynamic force due to the sediment ($\mathbf{f}_h^{(sed)}$) have normal and tangential components (Fig. 6),

$$\begin{array}{l} \mathbf{v} = \mathbf{v}_n + \mathbf{v}_\tau, \ \mathbf{v}_n = (\mathbf{v} \bullet \mathbf{n}) \mathbf{n}, \\ \mathbf{f}_h^{(sed)} = \mathbf{f}_n^{(sed)} + \mathbf{f}_\tau^{(sed)}, \end{array} \quad (28)$$

where $\mathbf{n}$ is the normal unit vector (outward positive); $\mathbf{v}_n$ and $\mathbf{v}_\tau$ are normal and tangential components of $\mathbf{v}$; $\mathbf{f}_n^{(sed)}$ and $\mathbf{f}_\tau^{(sed)}$ are the resistant forces in the normal and tangential directions. Note that the unit tangential vector $\boldsymbol{\tau}$ is in the opposite direction of $\mathbf{v}_\tau$. Let $B(z)$ and $S(z)$ be the sediment bulk density and shear strength profiles. As the cylinder penetrates into the sediment, the impact (resistant) force exerted on the part of the object's surface moving towards the sediment (Fig. 7),

$$\mathbf{f}_n^{(sed)}(z) = -\mathbf{n} \{ \int_{z_{ws}}^{z} [B(z') - \rho_w] dz' + S(z) \} \delta, \quad (29)$$

where ρ_w is water density and δ is a step function

$$\delta = \begin{cases} 1 & \mathbf{v}\bullet\mathbf{n} \geq 0 \\ 0 & \mathbf{v}\bullet\mathbf{n} \leq 0 \end{cases}. \quad (30)$$

Since the sediment is quasi-solid, the resistant force in the tangent direction ($\mathbf{f}_\tau^{(sed)}$) may be treated as the friction between two solid bodies that is proportional to the resistant force in the normal direction,

$$\mathbf{f}_\tau^{(sed)} = \boldsymbol{\tau} C \left| \mathbf{f}_n^{(sed)} \right|, \quad (31)$$

where C is the friction coefficient (0.01) between the cylinder and sediment. The total surface force due to sediment is calculated by

$$\begin{aligned} \mathbf{F}_h^{(sed)} &= \iint_{\sigma_{sed}} [\mathbf{f}_n^{(sed)} + \mathbf{f}_\tau^{(sed)}] d\sigma, \\ \mathbf{M}_h^{(sed)} &= \iint_{\sigma_{sed}} [\mathbf{r} \times (\mathbf{f}_n^{(sed)} + \mathbf{f}_\tau^{(sed)}) d\sigma, \end{aligned} \quad (32)$$

where σ_{sed} is the area of the cylinder's surface contacting with the sediment.

8. Model Integration

The momentum equation (7) and moment of momentum equation (8) are integrated numerically using the triple coordinate transformation ([2] Chu et al. 2004). As the cylinder penetrates into the sediment, the resistant force due to sediment $\mathbf{f}_h^{(sed)}$ reduces the cylinder's speed and turning angle. The vertical coordinate of COM [i.e., $z(t)$] in the E-coordinate and the elevation angle $\psi_2(t)$ are used to identify the cylinder's final burial depth and orientation,

$$\frac{dz}{dt} = 0, \quad \frac{d\psi_2}{dt} = 0. \quad (33)$$

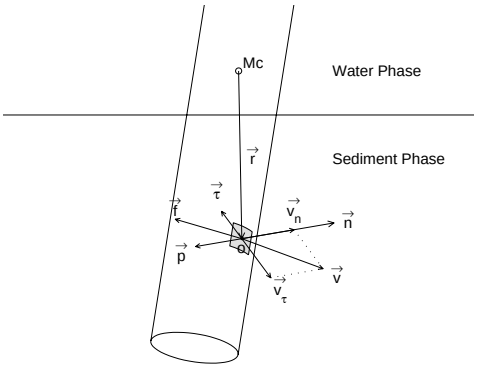

Fig. 6. Momentum and angular momentum balance for cylinder's penetration through the water-sediment interface.

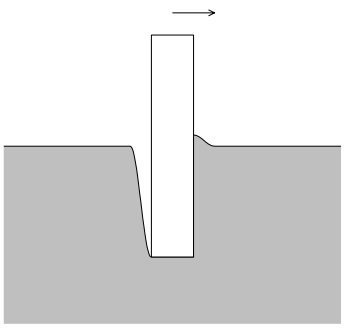

Fig. 7. The impact (resistant) force exerted on the part of the object's surface moving towards the sediment.

9. Cylinder Drop Experiments

Two cylinder drop experiments were conducted to collect data for the model evaluation. Exp-1 was designed to collect data on cylinder's motion in the water column for various combinations of the cylinder's parameters. Exp-2 was designed to collect synchronized data on sediment parameters (shear strength and density) and the cylinder's burial depth and orientation.

9.1. Exp-1

Exp-1 was conducted at the NPS swim pool in June 2001. It consisted of dropping each of three model cylinders (Fig. 8) into the water where each drop was recorded underwater from two viewpoints. The physical parameters of the model cylinders are listed in Table 1. Fig. 9 depicts the overall setup. The controlled parameters for each drop were: L/R ratio, χ-value, initial velocity ($\mathbf{V}_{in}$), and drop angle. The E-coordinate system is chosen with the origin at the corner of the swimming pool with the two sides as x- and y-axes and the vertical z-axis. The initial injection of cylinders was in the (y, z) plane (Fig. 10).

Initial velocity ($\mathbf{V}_{in}$) was calculated by using the voltage return of an infrared photo detector located at the base of the cylinder injector. The infrared sensor produced a square wave pulse when no light was detected due to blockage caused by the cylinder's passage. The length of the square wave pulse was converted into time by using a universal counter. Dividing the cylinder's length by the universal counter's time yielded $\mathbf{V}_{in}$. The cylinders were dropped from several positions within the injector mechanism in order to produce a range of $\mathbf{V}_{in}$. The method used to determine $\mathbf{V}_{in}$ required that the infrared light sensor be located above the water's surface. This distance was held fixed throughout the experiment at 10 cm.

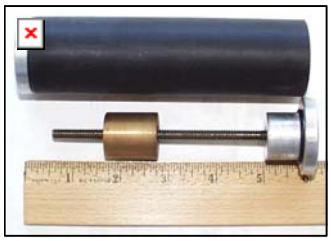

Fig. 8. Internal components of the model cylinder.

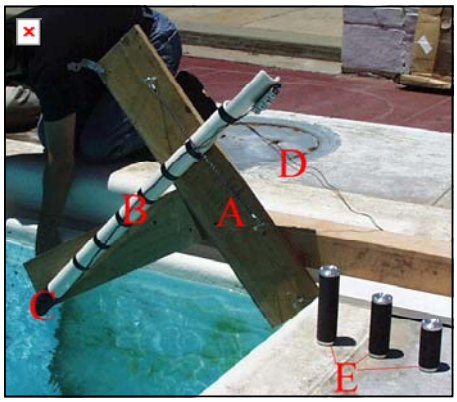

Fig. 9. Exp-1 equipments.

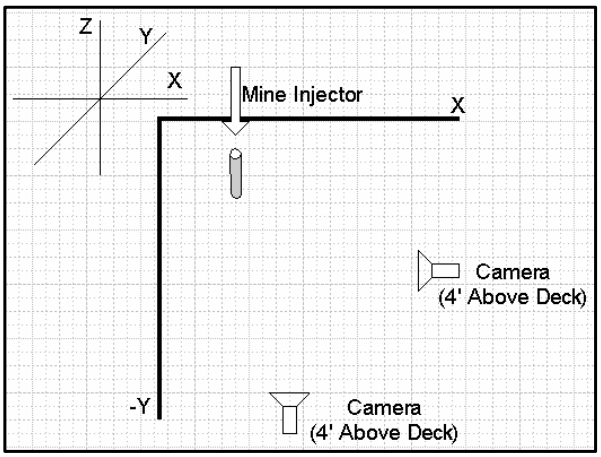

Fig. 10. Top view of Exp-1.

The drop angle (initial value of $\psi_2^{(in)}$) was controlled using the drop angle device. Five screw positions marked the 15°, 30°, 45°, 60°, and 75°. The drop angles were determined from the lay of the pool walkway, which was assumed to be parallel to the water's surface. A range of drop angles was chosen to represent the various entry angles that air and surface laid mines exhibit in naval operation. This range produced velocities whose horizontal and vertical components varied in magnitude. This allowed for comparison of cylinder trajectory sensitivity with the varying velocity components.

For each drop the cylinder was set to a χ-value. For positive χ-value, the cylinders were placed into the injector so that the COM was located below the geometric center. For negative χ-value, the COM was located above the geometric center to release. A series of drops were then conducted in order of decreasing mine length for each angle. Table 2 indicates number of drops conducted for different drop angles and χ-value for L/R = 15/2. Number of drops for other L/R ratios (12/2, 9/2) is comparable to that for L/R ratio of 15/2. All together there were 712 drops. Each video camera had a film time of approximately one hour. At the end of the day, the tapes were replayed in order to determine clarity and optimum camera position.

Upon completion of the drop phase, the video from each camera was converted to digital format. The digital video for each view was then analyzed frame by frame (30 Hz) in order to determine the mine's position in *x-z* and *y-z* planes. The cylinder's top and bottom positions were input into a MATLAB generated grid, similar to the ones within the pool. The first point to impact the water was always plotted first. This facilitated tracking of the initial entry point throughout the water column. The cameras were not time synchronized; thus, the first recorded position corresponded to when the full length of the mine was in view.

9.2. Exp-2

Exp-2 was conducted on the R/V John Martin on May 23, 2000. The barrel with density ratio of 1.8 was released while touching the surface. This would be to eliminate any chance of inertial effects caused by uneven introduction into the air-sea interface. This also set the initial velocity parameter in the code to zero. The barrel was to be released 17 times. The diver would snap the quick-release shackle on the barrel and then dive down to conduct measurements. The average depth of the water was 13 meters. Since it was uncertain the path the barrel would follow, both the releasing diver and a second safety diver would stay on the surface until after the barrel had dropped. Once reaching the bottom, one diver would take penetration measurements using a meter stick marked at millimeter increments while the other would take a gravity core. After 17 drops, the divers began to run out of air and results were not varying greatly so the decision was made to end the experiment. Upon return to the Monterey Bay Aquarium Research Institute, the gravity cores were taken immediately to the USGS Laboratories in Menlo Park, California where they were refrigerated until the analysis could be performed on May 31 – June 1, 2000.

Analysis of the gravity cores was begun on May 31, 2000 at the USGS Laboratories in Menlo Park, California. The gravity cores were sliced into two-centimeter segments to a depth of ten centimeters, and then sliced into four-centimeter segments. A Fall Cone Apparatus (Model G-200) was used to determine sediment shear strength.

In the test, it is assumed that the shear strength of sediment at constant penetration of a cone is directly proportional to the weight of the cone and the relation between undrained shear strength s and the penetration h of a cone of weight Q is given by:

$$S(z) = KQ / h^2, \qquad (34)$$

where K is a constant which depends mainly on the angle of the cone, but is also influenced by the sensitivity of the clay/sediment.

Table 1. Physical parameters of the model cylinders

Cylinder	Mass (g)	L (cm)	Volume (cm^3)	ρ_m ($g\ m^{-3}$)	J_1 ($g\ m^2$)	χ (cm)	J_2 (J_3) ($g\ m^2$)
1	322.5	15.20	191.01	1.69	330.5	0.00	6087.9
						0.74	5783.0
						1.48	6233.8
2	254.2	12.10	152.05	1.67	271.3	0.06	3424.6
						0.53	3206.5
						1.00	3312.6
3	215.3	9.12	114.61	1.88	235.0	0.00	1695.2
						0.29	1577.5
						0.58	1556.8

Table 2. Number of drops conducted for different drop angles and χ-values for L/R = 15/2.

$\psi_2^{(in)}$	15°	30°	45°	60°	75°
χ_2	13	15	15	15	12
χ_1	9	15	15	15	9
χ_0	12	14	15	18	6
χ_{-1}	0	6	6	6	0
χ_{-2}	2	6	6	0	0

Four different cones are used with this instrument, each one having the measuring range listed in Table 3. The cones are suspended from a permanent magnet. By pressing a knob, the magnet is moved so that the magnetic field is broken momentarily, and the cone is released. Measurements are taken of penetration depth and the evolution is repeated five times per sediment slice. These values are then averaged and correlated with a table which gives shear strength. Previous studies (Chu et al. 2002) showed that the sediment parameters are the most critical element in determining how deep an object was buried when it came to rest. During the experiment at the Monterey Bay, we obtained 17 gravity cores. Sediment bulk density and shear strength profiles (Fig. 11) show generally increase with depth until approximately 6-9 cm below the water-sediment interface.

Table 3. Measuring ranges of the gravity cores

Weight (g)	Apex-Angle	Penetration (mm)	Undrained shear strength (kPa)
400	30°	4.0 – 15.0	25 – 1.8
100	30°	5.0 – 15.0	4 – 0.45
60	60°	5.0 – 15.0	0.6 – 0.067
10	60°	5.0 – 20.0	0.10– 0.0063

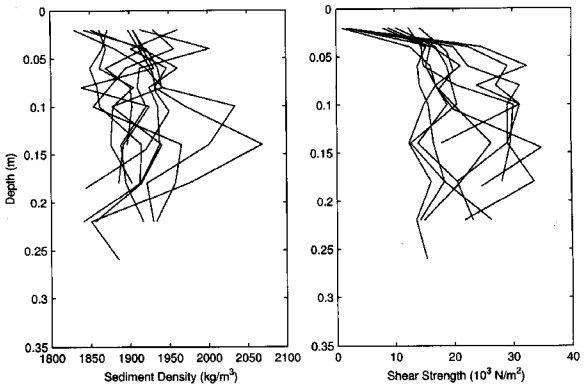

Fig. 11. Sediment density and shear strength profiles in the Monterey Bay collected during the cylinder drop experiment on May 31, 2000.

10. Model-Data Comparison

The U.S. Navy has a 2D model in x-z plane (IMPACT28) to predict cylinder's trajectory and impact burial. Since the motion of cylinder is 3D, the impact burial prediction using the 2D model has large errors (Chu et al., 2000). In this study, a new 3D model (called IMPACT35) is developed on the base of momentum balance (7) and moment of momentum balance (8) using triple coordinate transform ([2] Chu et al. 2004) and cylinder decomposition. To evaluate the value-added of the 3D model, comparison among the observed data (from Exp-1 and Exp-2) and predicted data using 2D (IMPACT28) and 3D (IMPACT35) models is conducted.

10.1. Comparison Using Exp-1 Data

Improvement from IMPACT28 to IMPACT35 in predicting cylinders' trajectory and orientation in the water column is verified using the Exp-1 data. Here, we list two examples.

Positive χ (Nose-Down): Cylinder #1 (L = 15.20 cm, $\rho = 1.69$ g cm^{-3}) with $\chi = 0.74$ cm is injected to the water with the drop angle 45^o. The physical parameters of this cylinder are given by

$$m = 322.5 \text{ g}, \quad J_1 = 330.5 \text{ g cm}^2, \; J_2 = J_3 = 5783.0 \text{ g cm}^2. \tag{35a}$$

Undersea cameras measure the initial conditions

$$x_0 = 0,\ y_0 = 0,\ z_0 = 0,$$
$$u_0 = 0,\ v_0 = -1.55 \text{ m s}^{-1},\ w_0 = -2.52 \text{ m s}^{-1},$$
$$\psi_{10}=0,\ \psi_{20} = 60^o,\ \psi_{30} = -95^o,$$
$$\omega_{10} = 0,\ \omega_{20} = 0.49 \text{ s}^{-1},\ \omega_{30} = 0.29 \text{ s}^{-1}. \tag{35b}$$

Substitution of the model parameters (35a) and the initial conditions (35b) into IMPACT28 and IMPACT35 leads to the prediction of the cylinder's translation and orientation that are compared with the data collected during Exp-1 at time steps (Fig. 12). The new 3D model (IMPACT35) simulated trajectory agrees well with the observed trajectory. Both show the same slant-straight pattern and the same travel time (1.23 s) for the cylinder passing through the water column. However, the existing 2D model (IMPACT28) has less capability to predict the cylinder's movement in the water column. The travel time predicted by IMPACT28 is 1.5 s, much more than the observed value.

Negative χ (Nose-Up): Cylinder #2 (L = 12.10 cm, $\rho = 1.67$ g cm^{-3}) with χ = -1.00 cm is injected to the water with the drop angle 30^o. The physical parameters of this cylinder are given by

$$m = 254.2 \text{ g}, \quad J_1 = 271.3 \text{ g cm}^2, \; J_2 = J_3 = 3312.6 \text{ g cm}^2. \tag{36a}$$

Undersea cameras measure the initial conditions

$$x_0 = 0,\ y_0 = 0,\ z_0 = 0,$$
$$u_0 = 0,\ v_0 = -0.75 \text{ m s}^{-1},\ w_0 = -0.67 \text{ m s}^{-1},$$
$$\psi_{10}=0,\ \psi_{20} = 24^o,\ \psi_{30} = -96^o,$$
$$\omega_{10} = 0,\ \omega_{20} = -5.08 \text{ s}^{-1},\ \omega_{30} = 0.15 \text{ s}^{-1}. \tag{36b}$$

The predicted cylinder's translation and orientation are compared with the data collected during Exp-1 at time steps (Fig. 13). The new 3D model (IMPACT35) simulated trajectory agrees well with the observed trajectory. Both show the same flip-spiral pattern and the same travel time (1.73 s) for the cylinder passing through the water column. The flip occurs at 0.11 s (0.13 s) after cylinder entering the water in the experiment (IMPACT35). After the flip, the cylinder spirals down to the bottom. However, the existing 2D model (IMPACT28) does not predict the flip-spiral pattern.

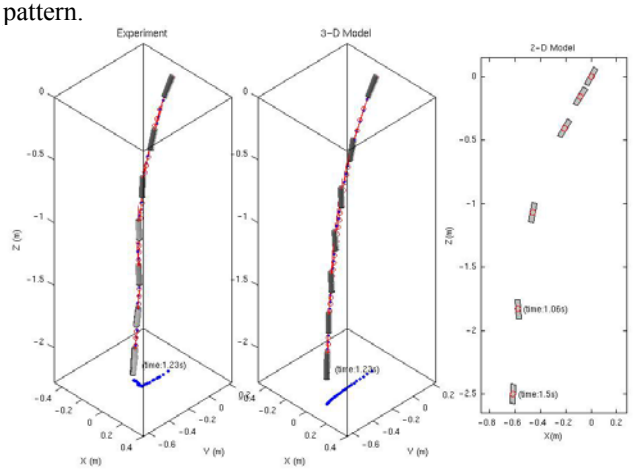

Fig. 12. Movement of Cylinder #1 (L = 15.20 cm, $\rho = 1.69$ g cm^{-3}) with χ = 0.74 m and drop angle 45^o obtained from (a) experiment, (b) 3D IMPACT35 model, and (c) 2D Impact28 model.

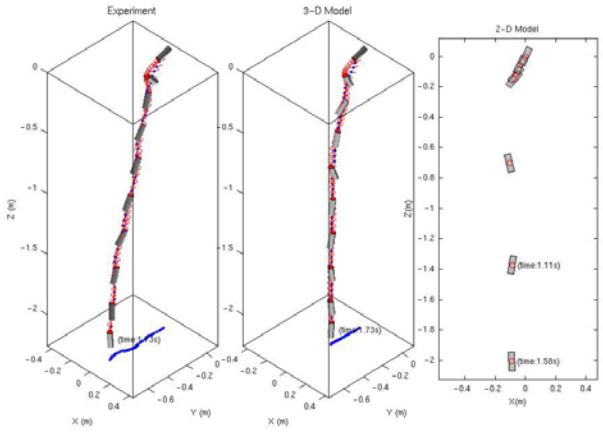

Fig. 13. Movement of Cylinder #2 (L = 12.10 cm, $\rho = 1.67$ g cm^{-3}) with χ = -1.00 cm and drop angle 30^o obtained from (a) experiment, (b) 3D IMPACT35 model, and (c) 2D Impact28 model.

10.2. Comparison Using Exp-2 Data

After running the two models (IMPACT35 and IMPACT28) for each gravity core regime and location, the burial depths were compared with measured burial depth data (Fig. 14). As evident, IMPACT35 improves the prediction capability. The existing 2D model (IMPACT25) over predicts actual burial depth by an order of magnitude on average. However, the 3D model (IMPACT35) predicts

the burial depth reasonably well. Since the gravity cores were taken for approximately two to three meters from the impact location, several cores were taken for each drop. This allowed an average to be calculated in order to yield more accurate data for each drop.

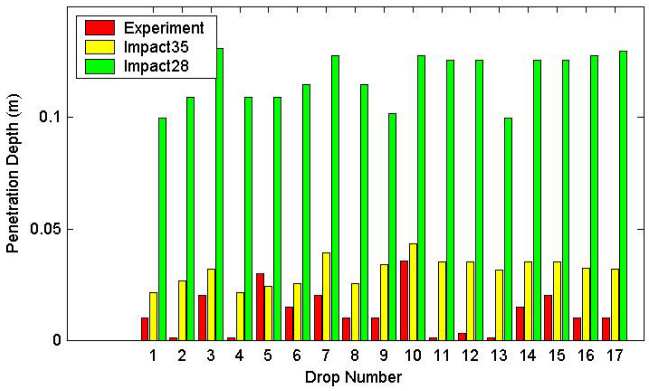

Fig. 14. Comparison among observed and predicted burial depths.

11. Conclusions

(1) A 3D Navy's model for Mine Impact Burial Prediction (IMPACT35) is developed to predict the translation and orientation of falling rigid cylinder through air, water, and sediment. It contains three components: triple coordinate transform, cylinder decomposition, and hydrodynamics of falling rigid object in a single medium (air, water, or sediment) and in multiple media (air-water and water-sediment interfaces).

(2) Triple coordinate transform is useful for modeling the movement of rigid body in air-water-sediment. The body forces (including buoyancy force) and torques are represented in the E-coordinate system, the hydrodynamic forces (such as the drag and lift forces) and torques are represented in the F-coordinate, and the cylinder's moments of gyration are represented in the M-coordinate. The momentum (moment of momentum) equation for predicting the cylinder's translation velocity (orientation) is represented in the E-coordinate (M-coordinate) system. Transformations among the three coordinate systems are used to convert the forcing terms into E-coordinate (M-coordinate) for the momentum (moment of momentum) equation.

(3) Cylinder decomposition proposed in this study leads to effective computation of the forces and torques as the cylinder penetrates an interface between two media. Volume decomposition is used to compute body forces and torques. The surface decomposition is used to calculate hydrodynamic forces and torques.

(4) Two cylinder drop experiments were conducted to evaluate the 3D model. Model-data comparison shows that IMPACT35 improves the prediction capability.

(5) Future work includes extension of IMPACT35 for cylindrical mines (current status) to any shapes of mines, and verification of IMPACT35 using the Navy's real-time mine warfare exercise data as well as other data regarding the movement of rigid objects (such as bombs) in the air-water-sediment.

Acknowledgments

The Office of Naval Research Marine Geosciences Program (N0001403WR20178), Naval Oceanographic Office, and the Naval Postgraduate School supported this study.

References

Arnone, R. A., and Bowen, Prediction Model of the Time History Penetration of a Cylinder through the Air-Water-Sediment Phases. NCSC letter report T34, Naval Coastal Systems Center, Panama City, FL, 1980.

Boorda, J. M., "Mine Countermeasures - An Integral Part of our Strategy and our Forces." Federation of American Scientists. (http://www.fas.org/man/dod-101/sys/ship/weaps/docs/cnopaper.htm)

Chu, P.C., E. Gottshall, and T.E. Halwachs, 1998: Environmental Effects on Naval Warfare Simulations. Institute of Joint Warfare Analysis, Naval Postgraduate School, Technical Report, NPS-IJWA-98-006, 33p.

Chu, P.C., V.I. Taber, and S.D. Haeger, 2000a: A Mine Impact Burial Model Sensitivity Study. Institute of Joint Warfare Analysis, Naval Postgraduate School, Technical Report, NPS-IJWA-00-003, 48p.

Chu, P.C., V.I. Taber, and S.D. Haeger, 2000b: Environmental Sensitivity Study on Mine Impact Burial Prediction Model. Proceedings on the Fourth International Symposium on Technology and the Mine Problem, 10 pp.

Chu, P.C., T.B. Smith, and S.D. Haeger, 2001: Mine burial impact prediction experiment. Institute of Joint Warfare Analysis, Naval Postgraduate School, Technical Report, NPS-IJWA-01-007, 161p.

Chu, P.C., A.F. Gilles, C.W. Fan, J. Lan, and P. Fleischer, 2002a: Hydrodynamics of falling cylinder in water column. Advances in Fluid Mechanics, 4, 163-181.

Chu, P.C., T.B. Smith, and S.D. Haeger, 2002b: Mine impact burial prediction experiment. Journal of Counter-Ordnance Technology (CD Rom).

Chu, P.C., A.F. Gilles, C.W. Fan, and P. Fleischer, 2002c: Hydrodynamics of falling mine in water column. Journal of Counter-Ordnance Technology (CD Rom).

Chu, P.C., C.W. Fan, A.D. Evans, and A. Gilles, 2003: Triple coordinate transforms for prediction of falling cylinder through the water column. Journal of Applied Mechanics, in press.

Hurst, R.B. Mine Impact Burial Prediction Model - Technical Description of Recent Changes and Developments. Defense Scientific Establishment, Auckland, New Zealand, Report 149.

Lehr, S.E., Mine Warfare: To Enable Maneuver, Amphibious Warfare Conference, 26 April 2000. (http:// www.exwar.org/awcfinal/6th/n852mines.ppt)

Lott, D.F., K. Williams, and D. Jackson, Mine Burial in Carbonate Sediments. Proc. of the Technology and Mine Problem Symposium, November 1996, Naval Postgraduate School.

Rhodes, J.E., G. Holder, Concept for Future Naval Mine Countermeasures in Littoral Power Projection, 1 May 1998. (http:// 192.156.75.102/mcm.htm)

Satkowiak, L. J., User's Guide for the Modified Impact Burial Prediction Model. NCSC TN 884-87. Naval Coastal Systems Center, Panama City, Fl, 1987.